
Conditional neural control variates for variance reduction in Bayesian inverse problems

Ali Siahkoohi¹Hyunwoo Oh²¹Department of Computer Science, University of Central Florida²Department of Physics and Maryland Center for Fundamental Physics, University of Maryland

Abstract

Bayesian inference for inverse problems involves computing expectations under posterior distributions—e.g., posterior means, variances, or predictive quantities—typically via Monte Carlo (MC) estimation. When the quantity of interest varies significantly under the posterior, accurate estimates demand many samples—a cost often prohibitive for partial differential equation-constrained problems. To address this challenge, we introduce conditional neural control variates, a modular method that learns amortized control variates from joint model–data samples to reduce the variance of MC estimators. To scale to high-dimensional problems, we leverage Stein’s identity to design an architecture based on an ensemble of hierarchical coupling layers with tractable Jacobian trace computation. Training requires: (i) samples from the joint distribution of unknown parameters and observed data; and (ii) the posterior score function, which can be computed from physics-based likelihood evaluations, neural operator surrogates, or learned generative models such as conditional normalizing flows. Once trained, the control variates generalize across observations without retraining. We validate our approach on stylized and partial differential equation-constrained Darcy flow inverse problems, demonstrating substantial variance reduction, even when the analytical score is replaced by a learned surrogate.

capture the non-uniqueness of the solution. The Bayesian framework addresses this by characterizing the full posterior distribution over solutions consistent with the observed data and prior knowledge. Posterior samples then provide expectations of quantities of interest—e.g., posterior means, variances, and credible intervals. Computing these expectations requires evaluating integrals of the form $\mathbb{E}_{p_{\text{post}}(\mathbf{x}|\mathbf{y})}[h(\mathbf{x})]$, which are typically intractable in closed form. While Monte Carlo (MC) estimation replaces the integral with a sample average [Robert and Casella, 2004], its variance— $\text{Var}(h(\mathbf{x}))/N$ for N i.i.d. samples—can be prohibitively large when $h(\mathbf{x})$ varies significantly under the posterior. In partial differential equation (PDE)-constrained inverse problems, where each posterior sample requires a computationally expensive forward solve, this high variance translates into high computational cost.

Control variates offer a classical remedy [Fieller and Hartley, 1954, Robert and Casella, 2004]: given an auxiliary function $g(\mathbf{x})$ with zero expectation under the target distribution and positive correlation with $h(\mathbf{x})$, the controlled estimator $\mathbb{E}_{p_{\text{post}}(\mathbf{x}|\mathbf{y})}[h(\mathbf{x}) - g(\mathbf{x})]$ has lower variance while remaining unbiased. Stein’s identity [Stein, 1972] provides a systematic way to construct such zero-mean functions from the score function—i.e., the gradient of the log-density—of the target distribution. Building on this principle, control functionals [Oates et al., 2017] and the zero-variance principle [Assaraf and Caffarel, 1999] have demonstrated the effectiveness of score-based control variates for MC integration, and neural networks have been used to parameterize them in gradient estimation [Grathwohl et al., 2018], rendering [Müller et al., 2020], general MC integration [Wan et al., 2020], and lattice field theory [Bedaque and Oh, 2024, Oh, 2025]. While these methods achieve impressive variance reduction, they all require retraining for each new observation \mathbf{y} , precluding amortization—a crucial limitation when training of these control variates for every new observation is computationally prohibitive.

To address this limitation, we introduce conditional neural control variates (CNCV), a modular variance reduc-

1 INTRODUCTION

Quantifying uncertainty in the solution of inverse problems is of fundamental importance in many areas of science and engineering [Tarantola, 2005, Stuart, 2010]. Due to noise and ill-posedness, a single point estimate fails to

tion method for MC estimation of posterior expectations in Bayesian inverse problems. Our method requires: (i) joint samples (\mathbf{x}, \mathbf{y}) drawn from the prior predictive distribution—by sampling \mathbf{x} from the prior and computing $\mathbf{y} = \mathcal{F}(\mathbf{x}) + \epsilon$ —samples that are already available in simulation-based inference pipelines [Cranmer et al., 2020]; and (ii) the posterior score function $\nabla_{\mathbf{x}} \log p(\mathbf{x}|\mathbf{y})$, which can come from physics-based evaluations, neural operator surrogates [Li et al., 2021], or learned generative models [Rezende and Mohamed, 2015, Song and Ermon, 2019, Ho et al., 2020, Papamakarios et al., 2021, Baldassari et al., 2023]. Once trained, the control variates apply to any new observation \mathbf{y} without retraining, integrating seamlessly with simulation-based inference techniques.

A further challenge arises when scaling Stein-based control variates to high dimensions: computing the divergence of a general neural network—required by the construction in Section 3—involves $\mathcal{O}(d)$ backward passes or stochastic trace estimation [Hutchinson, 1990]. To address this, we introduce an ensemble of hierarchical affine coupling layers inspired by HINT [Kruse et al., 2021], each operating on a random permutation of the input dimensions. The triangular Jacobian structure enables exact divergence computation in a single forward pass. Each ensemble member captures different cross-dimension interactions through its permutation, and averaging yields control variates with high correlation across all components of the quantity of interest.

Our main contributions are: (i) we extend neural control variates to the conditional setting, yielding amortized control variates that integrate with any posterior sampler and score source; (ii) we introduce an ensemble of hierarchical coupling layers with random input permutations that enable exact divergence computation; and (iii) we validate CNCV on four inverse problems of increasing complexity—Gaussian, Rosenbrock, nonlinear, and PDE-constrained Darcy flow—demonstrating substantial variance reduction that generalizes across observations, even with learned scores.

2 BAYESIAN INVERSE PROBLEMS

We are concerned with estimating an unknown parameter $\mathbf{x} \in \mathcal{X} \subset \mathbb{R}^d$ from noisy observations $\mathbf{y} \in \mathcal{Y} \subset \mathbb{R}^m$ related through the forward model $\mathbf{y} = \mathcal{F}(\mathbf{x}) + \epsilon$, where $\mathcal{F} : \mathcal{X} \rightarrow \mathcal{Y}$ is the forward operator and $\epsilon \sim \mathcal{N}(\mathbf{0}, \sigma^2 \mathbf{I})$ is additive Gaussian noise. In the Bayesian framework [Tarantola, 2005, Kaipio and Somersalo, 2006], the posterior distribution is given by Bayes’ rule:

$$p_{\text{post}}(\mathbf{x}|\mathbf{y}) \propto p_{\text{like}}(\mathbf{y}|\mathbf{x}) p_{\text{prior}}(\mathbf{x}), \quad (1)$$

where $p_{\text{like}}(\mathbf{y}|\mathbf{x})$ is the likelihood, $p_{\text{prior}}(\mathbf{x})$ encodes prior beliefs on the unknown, and the normalizing constant is the marginal likelihood $p(\mathbf{y})$. For brevity, we write $p(\mathbf{x}|\mathbf{y}) \equiv p_{\text{post}}(\mathbf{x}|\mathbf{y})$ throughout. Since the posterior is generally in-

tractable, we must resort to sampling-based methods to extract information from it.

2.1 SAMPLING THE POSTERIOR

Extracting information from the posterior requires access to samples—and many modern posterior sampling methods rely on the *score function* $\nabla_{\mathbf{x}} \log p(\mathbf{x}|\mathbf{y})$, either explicitly or implicitly. By Bayes’ rule, the score decomposes as $\nabla_{\mathbf{x}} \log p(\mathbf{x}|\mathbf{y}) = \nabla_{\mathbf{x}} \log p_{\text{like}}(\mathbf{y}|\mathbf{x}) + \nabla_{\mathbf{x}} \log p_{\text{prior}}(\mathbf{x})$. Gradient-based MCMC methods—such as MALA and HMC [Roberts and Rosenthal, 1998, Neal, 2011]—use the score to construct Markov chains that converge to the posterior, but produce correlated samples and require burn-in. Conditional generative models offer an alternative: conditional normalizing flows (CNFs; Rezende and Mohamed, 2015, Papamakarios et al., 2021) learn an invertible map from a base distribution to the posterior, providing both i.i.d. samples and an explicit density from which the score is obtained by automatic differentiation. Diffusion models [Song and Ermon, 2019, Ho et al., 2020, Baldassari et al., 2023] directly parameterize the score via denoising score matching. When the forward operator \mathcal{F} is differentiable—or when its adjoint is available—the likelihood score can also be evaluated analytically [Louboutin et al., 2023]; when \mathcal{F} is expensive, a differentiable surrogate [Li et al., 2021] can approximate it. In all cases, the score of the sampling distribution is available as a byproduct. Our control variate construction (Section 3) exploits this observation, requiring only that the score corresponds to the sampling distribution.

2.2 MONTE CARLO ESTIMATION AND CONTROL VARIATES

Once posterior samples are available, the primary computational task is estimating expectations of quantities of interest $h : \mathcal{X} \rightarrow \mathbb{R}$:

$$\mathbb{E}_{p_{\text{post}}(\mathbf{x}|\mathbf{y})}[h(\mathbf{x})] = \int_{\mathcal{X}} h(\mathbf{x}) p_{\text{post}}(\mathbf{x}|\mathbf{y}) d\mathbf{x}. \quad (2)$$

These expectations provide statistical summaries—e.g., the posterior mean ($h(\mathbf{x}) = \mathbf{x}$), posterior variance ($h(\mathbf{x}) = (\mathbf{x} - \boldsymbol{\mu}_{\text{post}})^2$), or predictive quantities. Given N samples $\{\mathbf{x}_i\}_{i=1}^N \sim p(\mathbf{x}|\mathbf{y})$, the MC estimator $\widehat{\mathbb{E}}[h(\mathbf{x})] = \frac{1}{N} \sum_{i=1}^N h(\mathbf{x}_i)$ is unbiased with variance $\text{Var}(h(\mathbf{x}))/N$. When $\text{Var}(h(\mathbf{x}))$ is large, accurate estimates demand many samples. A control variate $g : \mathcal{X} \times \mathcal{Y} \rightarrow \mathbb{R}$ satisfying $\mathbb{E}_{p(\mathbf{x}|\mathbf{y})}[g(\mathbf{x}, \mathbf{y})] = 0$ yields the controlled estimator

$$\widetilde{\mathbb{E}}[h(\mathbf{x})] = \frac{1}{N} \sum_{i=1}^N (h(\mathbf{x}_i) - g(\mathbf{x}_i, \mathbf{y})), \quad (3)$$

which is also unbiased, with per-sample variance $\text{Var}(h - g) = \text{Var}(h) + \text{Var}(g) - 2\text{Cov}(h, g)$. When g is positively correlated with h and has moderate variance, $\text{Var}(h -$

$g) < \text{Var}(h)$ —i.e., the control variate reduces the per-sample variance. When the samples $\{\mathbf{x}_i\}_{i=1}^N$ are i.i.d. draws from the posterior—e.g., from a conditional generative model or independent importance sampling—the terms $h(\mathbf{x}_i) - g(\mathbf{x}_i, \mathbf{y})$ are themselves i.i.d., and the estimator variance is $\text{Var}(h - g)/N$. The control variate therefore reduces the constant factor from $\text{Var}(h)$ to $\text{Var}(h - g)$ while preserving the $1/N$ convergence rate. The challenge is constructing such zero-mean functions g systematically; our approach (Section 3) uses the score from the sampling distribution to build g via Stein’s identity.

3 CONDITIONAL NEURAL CONTROL VARIATES

The goal of this section is to present the CNCV construction. The key insight is to combine Stein’s identity—which guarantees zero expectation by construction—with a hierarchical coupling layer architecture that makes the required divergence computation tractable.

3.1 CONTROL VARIATE CONSTRUCTION VIA STEIN’S IDENTITY

Stein’s identity [Stein, 1972] states that for any smooth $\phi: \mathbb{R}^d \times \mathbb{R}^m \rightarrow \mathbb{R}^d$ satisfying appropriate boundary conditions (see Appendix A),

$$\mathbb{E}_{p(\mathbf{x}|\mathbf{y})}[\nabla_{\mathbf{x}} \cdot \phi(\mathbf{x}, \mathbf{y}) + \phi(\mathbf{x}, \mathbf{y}) \cdot \nabla_{\mathbf{x}} \log p(\mathbf{x}|\mathbf{y})] = 0. \quad (4)$$

The above expression immediately provides a family of control variates parameterized by ϕ :

$$g(\mathbf{x}, \mathbf{y}) = \nabla_{\mathbf{x}} \cdot \phi(\mathbf{x}, \mathbf{y}) + \phi(\mathbf{x}, \mathbf{y}) \cdot \nabla_{\mathbf{x}} \log p(\mathbf{x}|\mathbf{y}), \quad (5)$$

where $\nabla_{\mathbf{x}} \cdot \phi = \sum_{i=1}^d \partial \phi_i / \partial x_i$ denotes the divergence. By construction, $\mathbb{E}_{p(\mathbf{x}|\mathbf{y})}[g(\mathbf{x}, \mathbf{y})] = 0$ for all \mathbf{y} , ensuring that g could be used as a control variate.

We parameterize ϕ by a neural network $\phi_{\theta}: \mathbb{R}^{d+m} \rightarrow \mathbb{R}^d$; substituting into equation (5) yields g_{θ} . Unfortunately, computing $\nabla_{\mathbf{x}} \cdot \phi_{\theta} = \sum_{i=1}^d \partial \phi_{\theta,i} / \partial x_i$ for a general neural network requires d backward passes or stochastic trace estimation [Hutchinson, 1990]—a cost that becomes prohibitive in high dimensions, motivating the architecture below.

3.2 HIERARCHICAL COUPLING LAYER ARCHITECTURE

To address the computational challenge of the divergence, we parameterize ϕ_{θ} using the hierarchical invertible neural transport (HINT) architecture of Kruse et al. [2021], which organizes affine coupling layers [Dinh et al., 2017] in a recursive binary tree. At each node, the input is split into

two halves $\mathbf{x} = [\mathbf{x}_1, \mathbf{x}_2]$ with $\mathbf{x}_1 \in \mathbb{R}^{d_1}$, $\mathbf{x}_2 \in \mathbb{R}^{d_2}$, and transformed via an affine coupling:

$$\phi_{\theta}(\mathbf{x}, \mathbf{y}) = \begin{bmatrix} \mathbf{x}_1 \\ \mathbf{s}_{\theta}(\mathbf{x}_1, \mathbf{y}) \odot \mathbf{x}_2 + \mathbf{t}_{\theta}(\mathbf{x}_1, \mathbf{y}) \end{bmatrix} \quad (6)$$

Here, \mathbf{s}_{θ} and \mathbf{t}_{θ} are neural networks conditioned on \mathbf{y} , and \odot denotes elementwise multiplication. In the recursive tree, the upper half is first processed by its subtree, and the resulting output—rather than the raw \mathbf{x}_1 —conditions the coupling of the lower half; the coupled lower half is then processed by its own subtree. This continues until leaf nodes are reached at a prescribed depth. The recursive subdivision ensures that every dimension participates in at least one coupling, producing a lower-triangular Jacobian with all but one diagonal entry learnable.

At a single coupling node, the triangular structure yields diagonal elements $\partial \phi_{\theta,i} / \partial x_i = 1$ for i in the upper partition and $\partial \phi_{\theta,i} / \partial x_i = s_{\theta,i}(\mathbf{x}_1, \mathbf{y})$ for i in the lower partition. The divergence contribution from one node is thus

$$\sum_{i \in \mathbf{x}_2} s_{\theta,i}(\mathbf{x}_1, \mathbf{y}) + d_1, \quad (7)$$

where $d_1 = \dim(\mathbf{x}_1)$. The full-tree Jacobian diagonal is computed recursively: $\mathbf{d} = [\mathbf{d}_{\text{upper}}; \mathbf{s} \odot \mathbf{d}_{\text{lower}}]$, with $\mathbf{d} = \mathbf{1}$ at leaf nodes (see Appendix A). The divergence $\nabla_{\mathbf{x}} \cdot \phi_{\theta} = \mathbf{1}^{\top} \mathbf{d}$ is exact and obtained in a single forward pass.

Each hierarchical coupling tree ϕ_{θ} maps $\mathbf{x} \in \mathbb{R}^d$ to \mathbb{R}^d . Crucially, the full Jacobian diagonal $\text{diag}(\nabla_{\mathbf{x}} \phi_{\theta})$ is available from the recursive forward pass, enabling a *vector-valued* control variate for $\mathbf{h}(\mathbf{x}) \in \mathbb{R}^k$ using a single network:

$$\mathbf{g}_{\theta}(\mathbf{x}, \mathbf{y}) = \text{diag}(\nabla_{\mathbf{x}} \phi_{\theta}) + \phi_{\theta}(\mathbf{x}, \mathbf{y}) \odot \nabla_{\mathbf{x}} \log p(\mathbf{x}|\mathbf{y}), \quad (8)$$

In the above expression, \odot denotes elementwise multiplication and k denotes the dimension of the quantity of interest. Since the j -th component $g_{\theta,j} = \partial \phi_{\theta,j} / \partial x_j + \phi_{\theta,j} \cdot \nabla_{x_j} \log p(\mathbf{x}|\mathbf{y})$ is exactly the j -th term of the product rule expansion *before* summing over components (see Appendix A), each component independently has zero expectation: $\mathbb{E}_{p(\mathbf{x}|\mathbf{y})}[\mathbf{g}_{\theta}] = \mathbf{0}$. A single tree thus produces control variates for all k components simultaneously, without requiring a separate network per component.

While a single tree produces valid control variates, it is limited by its fixed binary subdivision pattern. To improve coverage, we use L independent ensemble members, each with its own parameters and a random permutation \mathbf{P}_{ℓ} applied to the input dimensions (outputs are mapped back before computing g_j). Since the trace is invariant under conjugation, $\text{tr}(\mathbf{P}_{\ell} \mathbf{J} \mathbf{P}_{\ell}^{-1}) = \text{tr}(\mathbf{J})$, each permuted tree still satisfies Stein’s identity (Appendix A), and different permutations capture complementary cross-dimension interactions. The averaged control variate

$$\mathbf{g}_{\text{ens}}(\mathbf{x}, \mathbf{y}) = \frac{1}{L} \sum_{\ell=1}^L \mathbf{g}_{\theta_{\ell}}(\mathbf{x}, \mathbf{y}) \quad (9)$$

preserves $\mathbb{E}_{p(\mathbf{x}|\mathbf{y})}[\mathbf{g}_{\text{ens}}(\mathbf{x}, \mathbf{y})] = \mathbf{0}$; we verify this empirically in Appendix A (Figure 12). We ablate the effect of ensemble size in Section 4.1.4.

3.3 TRAINING

Our purpose is to find parameters θ that minimize the total variance of the controlled estimator $\mathbf{h} - \mathbf{g}$. Since $\mathbb{E}_{p(\mathbf{x}|\mathbf{y})}[\mathbf{g}_{\theta}(\mathbf{x}, \mathbf{y})] = \mathbf{0}$ by Stein’s identity, we have

$$\mathbb{E}[\|\mathbf{h} - \mathbf{g}\|^2] = \sum_{j=1}^d \text{Var}(h_j - g_j) + \|\mathbb{E}[\mathbf{h}]\|^2, \quad (10)$$

where the second term is constant in θ . Expanding each component gives $\text{Var}(h_j - g_j) = \text{Var}(h_j) + \text{Var}(g_j) - 2\text{Cov}(h_j, g_j)$, so minimizing the MSE simultaneously penalizes large $\text{Var}(g_j)$ and rewards high $\text{Cov}(h_j, g_j)$ —automatically balancing the two contributions to variance reduction. This yields the training objective:

$$\{\theta_{\ell}^*\} = \arg \min_{\{\theta_{\ell}\}} \mathbb{E}[\|\mathbf{h} - \mathbf{g}_{\text{ens}}\|^2], \quad (11)$$

where the expectation is over $(\mathbf{x}, \mathbf{y}) \sim p(\mathbf{x}, \mathbf{y})$. In practice, the expectation is approximated using N training samples $\{(\mathbf{x}_i, \mathbf{y}_i)\}_{i=1}^N$ generated by sampling $\mathbf{x}_i \sim p_{\text{prior}}(\mathbf{x})$ and computing $\mathbf{y}_i = \mathcal{F}(\mathbf{x}_i) + \epsilon_i$. The score function $\nabla_{\mathbf{x}} \log p(\mathbf{x}_i|\mathbf{y}_i)$ is evaluated at each training pair using any of the sources described in Section 2.1.

3.4 INFERENCE

For a new observation \mathbf{y}_{obs} , we draw M posterior samples using any available sampler (cf. line 9 of Algorithm 1) and compute the variance-reduced estimate (line 15):

$$\widehat{\mathbb{E}}[\mathbf{h}(\mathbf{x})] = \frac{1}{M} \sum_{j=1}^M (\mathbf{h}(\mathbf{x}_j) - \mathbf{g}_{\text{ens}}(\mathbf{x}_j, \mathbf{y}_{\text{obs}})). \quad (12)$$

The entire inference procedure involves only neural network forward passes and score evaluations— L coupling layer and score evaluations per sample. When the dominant cost is the forward model—e.g., PDE solves—this overhead is negligible. Crucially, no retraining is required for new observations, maintaining full amortization.

4 NUMERICAL EXPERIMENTS

We validate the proposed CNCV framework on four inverse problems of increasing complexity. We first consider three stylized problems—Gaussian, Rosenbrock, and nonlinear—with tractable posterior scores, then scale to a PDE-constrained Darcy flow inverse problem where the score must be learned from data. Throughout, we report the *variance reduction factor* (VRF) = $\text{Var}(h - g)/\text{Var}(h)$,

Algorithm 1 Conditional neural control variates (CNCV)

Require: Prior p_{prior} , forward model \mathcal{F} , score source, posterior sampler, ensemble size L , quantity of interest \mathbf{h}

```

1: // Offline training
2: for  $i = 1, \dots, N_{\text{train}}$  do
3:   Sample  $\mathbf{x}_i \sim p_{\text{prior}}(\mathbf{x})$ 
4:   Compute  $\mathbf{y}_i = \mathcal{F}(\mathbf{x}_i) + \epsilon_i$ 
5:   Evaluate  $\nabla_{\mathbf{x}} \log p(\mathbf{x}_i|\mathbf{y}_i)$  from chosen score source
6: end for
7: Initialize  $L$  hierarchical coupling layers with random
   input permutations
8: Optimize  $\{\theta_{\ell}\}_{\ell=1}^L$  via equation (11)
9: // Online inference (for any new  $\mathbf{y}_{\text{obs}}$ )
10: Draw  $M$  posterior samples  $\{\mathbf{x}_j\}_{j=1}^M \sim p(\mathbf{x}|\mathbf{y}_{\text{obs}})$ 
11: for  $j = 1, \dots, M$  do
12:   Evaluate score  $\nabla_{\mathbf{x}} \log p(\mathbf{x}_j|\mathbf{y}_{\text{obs}})$ 
13:   Evaluate  $\mathbf{g}_{\text{ens}}(\mathbf{x}_j, \mathbf{y}_{\text{obs}})$  via equation (9)
14: end for
15: return  $\widehat{\mathbb{E}}[\mathbf{h}] = \frac{1}{M} \sum_{j=1}^M (\mathbf{h}(\mathbf{x}_j) - \mathbf{g}_{\text{ens}}(\mathbf{x}_j, \mathbf{y}_{\text{obs}}))$ 

```

Table 1: Variance reduction for Gaussian posteriors. VRF = $\text{Var}(h-g)/\text{Var}(h)$; lower is better. Values are mean \pm std across d components, each averaged over 100 observations.

d	Mean Est. VRF	Var. Est. VRF
2	0.030 \pm 0.005	0.022 \pm 0.008
4	0.040 \pm 0.011	0.020 \pm 0.012
8	0.076 \pm 0.023	0.073 \pm 0.043
16	0.150 \pm 0.086	0.267 \pm 0.258

where lower values indicate stronger variance reduction (VRF = 0 is perfect, VRF = 1 is no improvement). In all experiments, $k = d$ —i.e., the quantity of interest has the same dimension as the unknown parameter.

4.1 STYLIZED INVERSE PROBLEMS

These experiments quantify variance reduction and its effect on estimation accuracy, study how performance scales with dimension and sample size, ablate the ensemble size, and assess sensitivity to learned scores. Full hyperparameters are in Appendix E.

4.1.1 Gaussian posterior

Consider the inverse problem $\mathbf{y} = \mathbf{x} + \epsilon$ with $\mathbf{x} \in \mathbb{R}^d \sim \mathcal{N}(\mathbf{0}, \Sigma_{\text{prior}})$ and $\epsilon \sim \mathcal{N}(\mathbf{0}, \sigma^2 \mathbf{I})$ with $\sigma = 0.3$. The prior covariance matrix is a randomly generated positive definite matrix. The analytical posterior is Gaussian with known mean and covariance. We evaluate (i) posterior mean estimation with $\mathbf{h}(\mathbf{x}) = \mathbf{x}$, and (ii) posterior variance estimation with $\mathbf{h}(\mathbf{x}) = (\mathbf{x} - \boldsymbol{\mu}_{\text{post}})^2$.

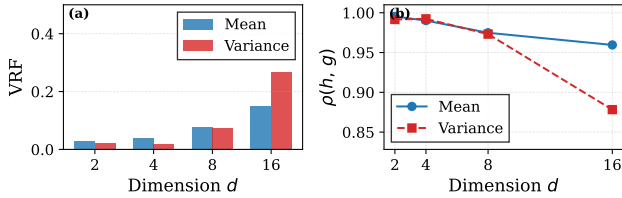


Figure 1: Dimension scaling of CNCV. (a) VRF for mean and variance estimation across $d \in \{2, 4, 8, 16\}$ (lower is better; VRF = 1 means no improvement). (b) Correlation between h and g across dimensions.

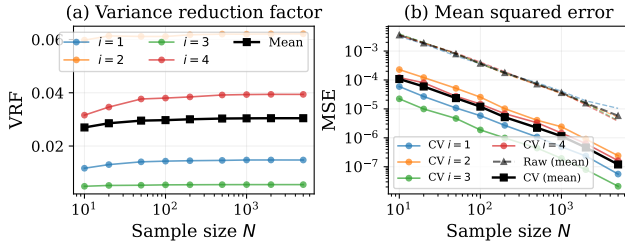


Figure 2: Sample efficiency for $d = 4$ mean estimation. (a) VRF is sample-size invariant at ~ 0.04 . (b) MSE follows $1/N$ rate; the CV estimator provides a $\sim 25\times$ effective sample increase. Index i denotes the component.

Table 1 summarizes results across dimensions. We observe that for mean estimation, CNCV achieves VRF between 0.03 and 0.15 across $d \in \{2, 4, 8, 16\}$, while for variance estimation, VRF remains below 0.08 at $d \leq 8$ and reaches 0.27 at $d = 16$ (each entry is averaged over 100 test observations). Figure 1 shows that VRF grows mildly with d , while correlation between h and g remains above 0.96 for mean estimation. The learned control variates achieve per-component correlation $\rho > 0.98$ with the target. Figure 2 shows the sample efficiency for $d = 4$. We observe from panel (a) that the VRF is sample-size invariant at ~ 0.04 across sample sizes from 10 to 5k. Panel (b) shows MSE vs. sample size: while both estimators follow the $1/N$ rate, the CV estimator has a substantially lower constant factor.

4.1.2 Rosenbrock posterior

To assess CNCV on non-Gaussian posteriors, we consider the Rosenbrock distribution—a benchmark with a strongly curved, banana-shaped density, with prior $p(\mathbf{x}) \propto \exp(-a(x_1 - \mu)^2 - b(x_2 - x_1^2)^2)$ where $\mu = 0, a = 0.5, b = 1$. Combined with Gaussian likelihood $p(\mathbf{y}|\mathbf{x}) = \mathcal{N}(\mathbf{x}, \sigma^2 \mathbf{I})$ with $\sigma = 0.3$, the posterior is non-Gaussian and exhibits strong nonlinear correlations between components.

Figure 3 demonstrates amortization across three test observations from diverse regions: $\mathbf{y}^{(1)}$ from the left tail, $\mathbf{y}^{(2)}$ from the right tail at high x_2 , and $\mathbf{y}^{(3)}$ near the ridge. Each observation (marked by stars) induces a differently posi-

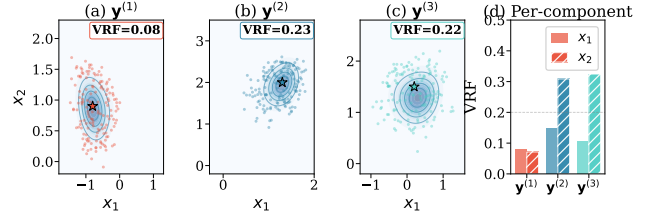


Figure 3: Amortized CNCV on Rosenbrock posterior. (a–c) Test observations from left tail, right tail, and ridge (stars) yield diverse posteriors; VRF values are shown in each panel. (d) Per-component VRF for each observation; the same trained model achieves $\text{VRF} \in [0.08, 0.23]$ across all cases (lower is better).

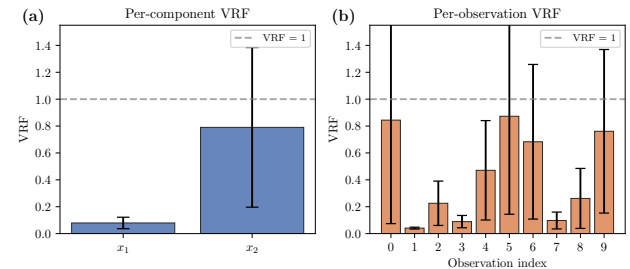


Figure 4: Posterior variance estimation on the Rosenbrock problem. (a) Per-component VRF: x_1 achieves strong reduction while x_2 (banana direction) is harder. (b) Per-observation VRF across 10 test observations (mean 0.44).

tioned banana-shaped posterior. Despite this diversity, the *same trained model* achieves VRF between 0.08 and 0.23 across all cases (panel d). This confirms that the control variate generalizes to any new observation.

Aside from posterior mean estimation, CNCV also reduces variance for posterior variance estimation. Figure 4 uses $\mathbf{h}(\mathbf{x}) = (\mathbf{x} - \boldsymbol{\mu}_{\text{est}})^2$, where $\boldsymbol{\mu}_{\text{est}}$ and the score are obtained from a pretrained CNF (Section 2.1). The first component (x_1) achieves $\text{VRF} = 0.08$, while the banana direction (x_2)—where the posterior exhibits the strongest nonlinear correlations—is harder ($\text{VRF} = 0.79$), yielding a mean VRF of 0.44 across 10 test observations.

4.1.3 Nonlinear forward model

We next consider the nonlinear forward model $\mathcal{F}(\mathbf{x}) = \mathbf{A}\mathbf{x} + \sin(\mathbf{x})$ in $d = 4$, where \mathbf{A} has condition number 2. Figure 5 shows the non-Gaussian posteriors for three test observations. At test time, posterior samples come from a denoising diffusion probabilistic model [Ho et al., 2020] trained on the same joint distribution, providing fast amortized sampling. CNCV achieves $\text{VRF} = 0.57 \pm 0.29$ across 10 test observations. Figure 6 shows the per-component and per-observation VRFs.

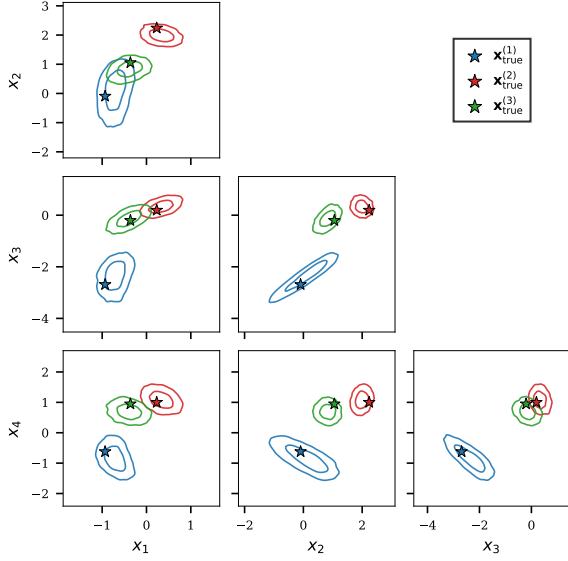


Figure 5: Corner plot of the nonlinear posterior ($d = 4$) for three test observations (blue, red, green). Contours show 50% and 90% HDRs; stars mark the true parameters.

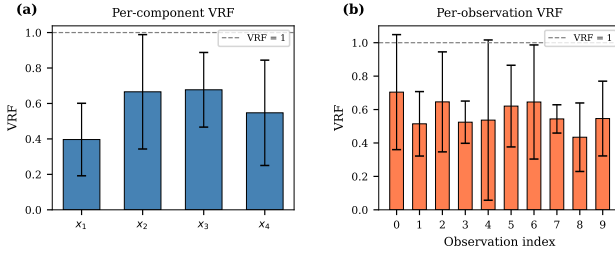


Figure 6: CNCV variance reduction on the nonlinear forward model ($d = 4$). (a) Per-component VRF averaged over 10 test observations. (b) Per-observation VRF (mean 0.57).

4.1.4 Training efficiency and ensemble size

Figure 7(a) shows VRF versus total training samples seen for both the Gaussian ($d = 4$) and Rosenbrock ($d = 2$) problems. We observe that both converge rapidly: the Gaussian VRF drops from ~ 19 to below 0.03, and the Rosenbrock from ~ 277 to below 0.14, within the first few passes over the dataset. Figure 7(b) shows VRF as a function of the ensemble size L . A single member ($L = 1$) yields almost no variance reduction; however, two members already reduce VRF by two orders of magnitude on the Gaussian problem, and performance saturates beyond $L \approx 8$. This motivates the default $L = 16$ used throughout our experiments.

4.1.5 Sensitivity to learned scores

All preceding experiments used posterior scores computed directly from the known likelihood and prior. In practice, however, the score must often be learned from data—

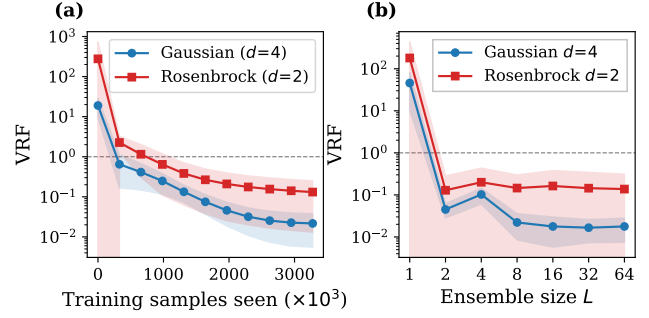


Figure 7: (a) VRF versus total training samples seen. (b) VRF versus ensemble size L . Shading shows ± 1 standard deviation across test observations. Both panels show Gaussian $d = 4$ and Rosenbrock $d = 2$ mean estimation.

Table 2: Analytical vs. CNF-learned score comparison. VRF = $\text{Var}(h-g)/\text{Var}(h)$; lower is better. Gaussian and nonlinear: mean \pm std across components; Rosenbrock: range over three test observations. Each ensemble is trained and evaluated with the same score source.

Problem	Score	VRF	Red. (%)	ρ
Gauss. $d=4$	Analyt.	0.040 ± 0.011	96	>0.99
Gauss. $d=4$	CNF	0.058 ± 0.002	94	0.98
Rosenb. $d=2$	Analyt.	0.08–0.23	77–92	—
Rosenb. $d=2$	CNF	0.010 ± 0.002	99	>0.99
Nonlin. $d=4$	Analyt.	0.57 ± 0.29	43	—
Nonlin. $d=4$	CNF	0.57 ± 0.26	43	—

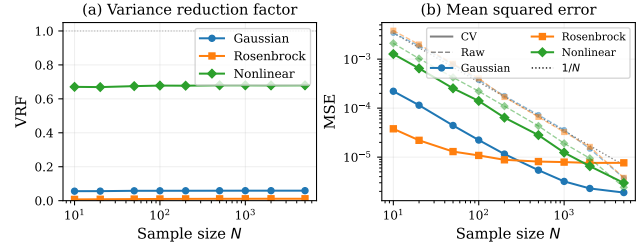


Figure 8: Sample efficiency with CNF-learned scores. (a) VRF is sample-size invariant. (b) The CV estimator (solid) provides a constant-factor MSE improvement over raw MC (dashed). MSE plateaus at large N due to residual bias from the CNF score approximation.

particularly for inverse problems governed by expensive PDEs, where amortized inference is often the only computationally viable option. To assess robustness to score approximation error, we train a CNF to approximate $p(\mathbf{x}|\mathbf{y})$ via negative log-likelihood on joint samples drawn from $p(\mathbf{x}, \mathbf{y})$. The score is then obtained by automatic differentiation of the change-of-variables log-density (CNF architecture details in Appendix E). As discussed in Section 2.1, using the CNF score together with CNF samples yields an estimator unbiased for $\mathbb{E}_{p_\varphi} [h(\mathbf{x})]$ —i.e., expectations under the learned

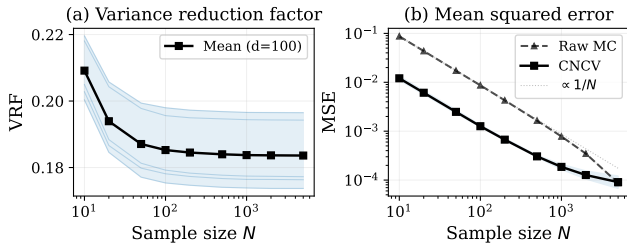


Figure 9: Sample efficiency for Darcy flow. (a) VRF is sample-size invariant at ~ 0.18 . (b) MSE of the posterior mean estimator follows $1/N$ for both raw MC and CNCV, with the CV estimator achieving a $\sim 5.5\times$ constant-factor improvement. At large N , both curves plateau because the reference mean is estimated from a finite CNF sample pool.

posterior rather than the true posterior. MSE in Figure 8 is accordingly computed against the CNF sample mean. Table 2 compares analytical and CNF-learned scores on all three benchmarks. On the Gaussian problem ($d=4$), the CNF score increases VRF from 0.040 to 0.058—a modest degradation consistent with score approximation error. On the Rosenbrock problem ($d=2$), the CNF score achieves VRF of 0.010 ± 0.002 with $\rho > 0.99$, lower than the analytical-score VRF (0.08–0.23)—likely because the CNF provides i.i.d. samples, whereas the analytical-score experiment relies on correlated MCMC draws. On the nonlinear problem ($d=4$), the CNF score achieves $\text{VRF} = 0.57 \pm 0.26$, virtually identical to the analytical score (0.57 ± 0.29), despite 17.5% relative score error. These results suggest that the coupling layer architecture is robust to moderate score approximation errors. Figure 8 confirms that VRF remains sample-size invariant with CNF-learned scores, and the CV estimator maintains a constant-factor MSE improvement over raw MC across all sample sizes.

4.2 PDE-CONSTRAINED INVERSE PROBLEM

We now apply CNCV to a higher-dimensional, PDE-constrained problem: estimating the log-permeability field in a groundwater flow model governed by Darcy’s equation [Darcy, 1856], $-\nabla \cdot (e^{u(s)} \nabla p(s)) = 0$ on $\mathcal{D} = [0, 1]^2$, with mixed boundary conditions [Beskos et al., 2017]. The unknown log-permeability $u(s)$ is observed through $m = 33$ pressure sensors with Gaussian noise ($\sigma_y = 0.01$). The PDE forward model costs ~ 0.5 s per solve, the posterior is high-dimensional, and the score must be learned from data. Following Beskos et al. [2017], the prior on u is a Gaussian random field (GRF) represented via a cosine Karhunen–Loève (KL) expansion with truncation $K = 10$, giving $u(s) = \sum_{j=1}^{100} z_j \sqrt{\lambda_j} \psi_j(s)$ where λ_j are the GRF eigenvalues and ψ_j are cosine eigenfunctions. The training data consists of $d = K^2 = 100$ KL coefficients $\mathbf{z} \in \mathbb{R}^{100}$ obtained by expanding GRF samples, paired with the corresponding observations. The forward model reconstructs

the field from \mathbf{z} , solves the PDE on a 40×40 grid using Devito [Louboutin et al., 2019, Luporini et al., 2020], and extracts pressures at the sensor locations. Since the posterior score is not available in closed form for this nonlinear PDE, we train a CNF on 120k joint (\mathbf{z}, \mathbf{y}) samples to serve as both posterior sampler and score source (Appendix C verifies the quality of the learned score). The CNCV ensemble uses $L = 16$ depth-3 trees; full hyperparameters are in Appendix E.

Figure 9 confirms that the VRF is sample-size invariant at ~ 0.18 , with the CV estimator achieving $\sim 5.5\times$ lower MSE—an effective $5.5\times$ sample size increase on this 100-dimensional problem. Figure 10 shows the posterior summary for a held-out observation: the CNCV mean closely matches the truth, with posterior uncertainty concentrated in the domain interior—away from sensors and Dirichlet boundaries. Since the reconstruction is linear in the KL coefficients, the posterior standard deviation is governed by the sensor geometry rather than the specific observation values, and is therefore consistent across test cases (Appendix D). As observed from Figure 11, CNCV reduces estimator standard deviation most strongly along large-scale structures; per-observation VRF is tightly concentrated around 0.18 across 20 test observations.

5 RELATED WORK

Stein-based control variates have a rich history in MC variance reduction. The zero-variance principle of Assaraf and Caffarel [1999] inspired kernel-based control functionals [Oates et al., 2017, 2019, South et al., 2022] and polynomial/regularized MCMC estimators [Mira et al., 2013, South et al., 2023], while Si et al. [2022] unified polynomial, kernel, and neural function classes under a scalable Stein objective. Neural networks have also been used to parameterize control variates outside the Stein framework—for gradient estimation [Grathwohl et al., 2018], rendering [Müller et al., 2020], general MC integration [Wan et al., 2020], and vector-valued [Sun et al., 2023a] and meta-learning [Sun et al., 2023b] settings—and within it, for lattice field theory [Bedaque and Oh, 2024, Oh, 2025]. However, all of these methods are *non-amortized*: each must be fitted for a specific target distribution, requiring MCMC samples and an $\mathcal{O}(n^3)$ kernel solve [Oates et al., 2017], or least-squares regression on MCMC output [Mira et al., 2013].

In contrast, amortized methods train a single model that generalizes across observations [Blei et al., 2017]. Conditional normalizing flows [Rezende and Mohamed, 2015, Papamakarios et al., 2021] and simulation-based inference [Cramer et al., 2020, Radev et al., 2020] learn density estimators $p_\varphi(\mathbf{x}|\mathbf{y})$ from joint samples, with extensions to inverse problems [Siahkoobi et al., 2022, 2023, Orozco et al., 2025]; importance sampling can further reduce variance through better proposals [Dax et al., 2023], complementary to control

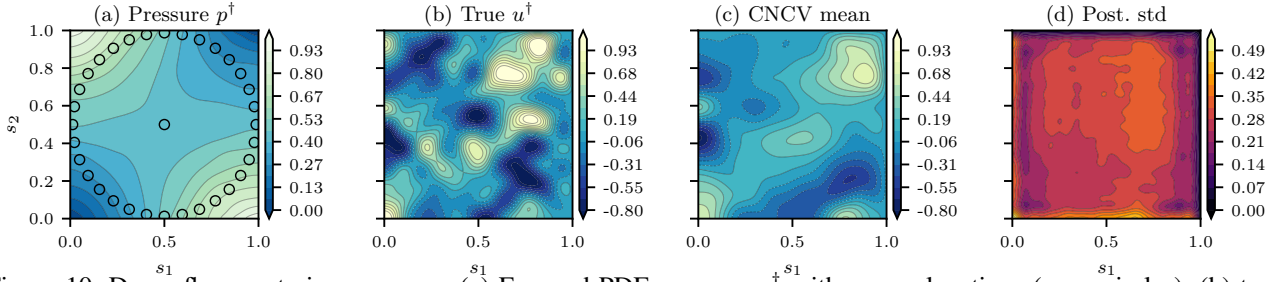


Figure 10: Darcy flow posterior summary. (a) Forward PDE pressure p^\dagger with sensor locations (open circles); (b) true log-permeability u^\dagger ; (c) CNCV posterior mean from $N = 5,000$ CNF samples; (d) pointwise posterior standard deviation. All fields reconstructed at 128×128 from KL coefficients.

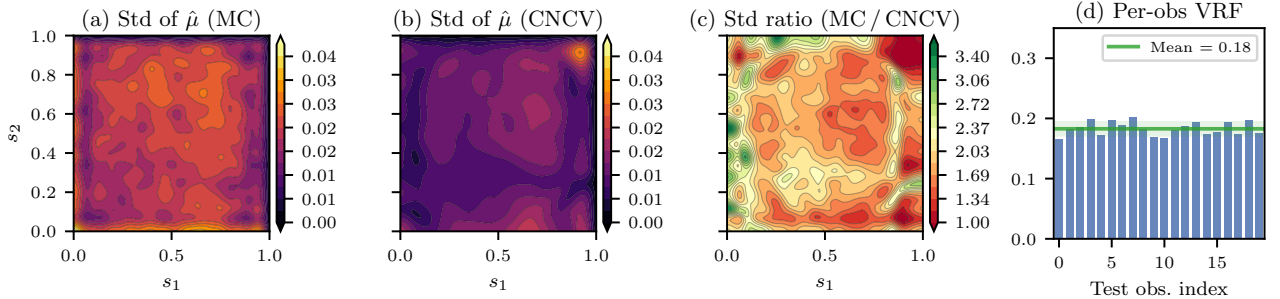


Figure 11: Variance of the mean estimator on the Darcy flow problem. (a, b) Pixelwise standard deviation of the posterior mean estimator $\hat{\mu} = \frac{1}{N} \sum_i \mathbf{x}_i$ for vanilla MC and CNCV; (c) std ratio (MC / CNCV), where values > 1 indicate that CNCV reduces estimator variance; (d) per-observation VRF across 20 held-out test observations.

variates. However, to our knowledge, no prior work has proposed *amortized control variates*—observation-conditioned functions $g(\mathbf{x}, \mathbf{y})$ with zero posterior expectation that generalize to unseen \mathbf{y} without retraining.

6 DISCUSSION

The proposed method integrates seamlessly with simulation-based inference techniques [Cranmer et al., 2020], which already produce joint samples $(\mathbf{x}_i, \mathbf{y}_i)$ and learned posterior approximations from which the score is readily available. CNCV training consumes exactly these existing artifacts, adding no extra forward model evaluations, and the inference-time cost of evaluating the ensemble of coupling layers is comparable to a single shallow network evaluation. At the same time, CNCV also accommodates physics-based scores computed directly from the likelihood and prior, making it applicable to problems where high-fidelity forward evaluations are available and accurate score computation is paramount. This flexibility makes CNCV attractive across a wide range of settings—from problems constrained by partial differential equations, where each forward solve dominates the computational budget and any variance reduction translates directly into proportional savings, to lower-cost problems where the analytical score is readily accessible.

It is worth noting that CNCV reduces the variance of posterior expectations computed from a given set of samples,

but does not alter the samples themselves or improve the underlying posterior approximation. While the quality of the control variate depends on score accuracy, our normalizing flow-based experiments demonstrate that learned scores yield comparable variance reduction to analytical scores. Since Stein’s identity requires the score to correspond to the sampling distribution, it is crucial that the score and posterior samples originate from the same source—e.g., both from a CNF—to preserve the zero-mean property of the control variate. For simple posteriors, polynomial control variates [Mira et al., 2013] can match CNCV for a single observation; however, the value of CNCV lies in non-Gaussian settings where amortization across observations is needed. As with any amortized method, we expect a gap relative to observation-specific optimization [Orozco et al., 2025]; CNCV is complementary to such refinement strategies and can be combined with them to further reduce estimator variance.

Aside from the inverse problems considered above, the principle of learning amortized, Stein-based control variates is applicable to other domains where Monte Carlo estimation is a computational bottleneck—e.g., variance reduction of policy gradient estimators in reinforcement learning [Green-Smith et al., 2004], scaling to higher-dimensional fields by operating in latent spaces learned by functional autoencoders [Bunker et al., 2025], and amortized uncertainty quantification for digital twins [Herrmann, 2023].

Related material

The Darcy flow forward solver relies on the Devito [Louboutin et al., 2019, Luporini et al., 2020] finite-difference compiler via a lightweight groundwater solver available at github.com/luqigroup/groundwater. Prior samples from the corrected Gaussian random field are generated using the code available at github.com/luqigroup/grf. Code to partially reproduce the results presented in this work is available at github.com/luqigroup/cncv.

Acknowledgements

Ali Siahkoohi acknowledges support from the Institute for Artificial Intelligence at the University of Central Florida.

References

- Roland Assaraf and Michel Caffarel. Zero-variance principle for Monte Carlo algorithms. *Physical Review Letters*, 83(23):4682, 1999.
- Lorenzo Baldassari, Ali Siahkoohi, Josselin Garnier, Knut Sølna, and Maarten V. de Hoop. Conditional score-based diffusion models for Bayesian inference in infinite dimensions. In *Advances in Neural Information Processing Systems*, volume 36, pages 24262–24290, 2023.
- Paulo F. Bedaque and Hyunwoo Oh. Leveraging neural control variates for enhanced precision in lattice field theory. *Physical Review D*, 109:094519, 2024.
- Alexandros Beskos, Mark Girolami, Shiwei Lan, Patrick E. Farrell, and Andrew M. Stuart. Geometric MCMC for infinite-dimensional inverse problems. *Journal of Computational Physics*, 335:327–351, 2017.
- David M. Blei, Alp Kucukelbir, and Jon D. McAuliffe. Variational inference: a review for statisticians. *Journal of the American Statistical Association*, 112(518):859–877, 2017.
- Justin Bunker, Mark Girolami, Hefin Lambley, Andrew M. Stuart, and T. J. Sullivan. Autoencoders in function space. *Journal of Machine Learning Research*, 26(165):1–54, 2025.
- Kyle Cranmer, Johann Brehmer, and Gilles Louppe. The frontier of simulation-based inference. *Proceedings of the National Academy of Sciences*, 117(48):30055–30062, 2020.
- Henry Darcy. *Les fontaines publiques de la ville de Dijon*. Victor Dalmont, Paris, 1856.
- Maximilian Dax, Stephen R. Green, Jonathan Gair, Michael Pürner, Jonas Wildberger, Jakob H. Macke, Alessandra Buonanno, and Bernhard Schölkopf. Neural importance sampling for rapid and reliable gravitational-wave inference. *Physical Review Letters*, 130:171403, 2023.
- Laurent Dinh, Jascha Sohl-Dickstein, and Samy Bengio. Density estimation using real NVP. In *International Conference on Learning Representations*, 2017.
- E. C. Fieller and H. O. Hartley. Sampling with control variables. *Biometrika*, 41:494–501, 1954.
- Will Grathwohl, Dami Choi, Yuhuai Wu, Geoffrey Roeder, and David Duvenaud. Backpropagation through the void: Optimizing control variates for black-box gradient estimation. In *International Conference on Learning Representations*, 2018.
- Evan Greensmith, Peter L. Bartlett, and Jonathan Baxter. Variance reduction techniques for gradient estimates in reinforcement learning. *Journal of Machine Learning Research*, 5:1471–1530, 2004.
- Felix J. Herrmann. Digital twins in the era of generative AI. *The Leading Edge*, 42(11):730–732, 2023.
- Jonathan Ho, Ajay Jain, and Pieter Abbeel. Denoising diffusion probabilistic models. In *Advances in Neural Information Processing Systems*, 2020.
- Michael F. Hutchinson. A stochastic estimator of the trace of the influence matrix for Laplacian smoothing splines. *Communications in Statistics – Simulation and Computation*, 19(2):433–450, 1990.
- Jari Kaipio and Erkki Somersalo. *Statistical and Computational Inverse Problems*. Springer, 2006.
- Diederik P. Kingma and Jimmy Ba. Adam: A method for stochastic optimization. In *International Conference on Learning Representations*, 2015.
- Jakob Kruse, Gianluca Detommaso, Robert Scheichl, and Ullrich Köthe. HINT: Hierarchical Invertible Neural Transport for Density Estimation and Bayesian Inference. In *AAAI Conference on Artificial Intelligence*, volume 35, pages 8191–8199, 2021.
- Zongyi Li, Nikola Kovachki, Kamyar Azizzadenesheli, Burigede Liu, Kaushik Bhatt, Andrew Stuart, and Anima Anandkumar. Fourier neural operator for parametric partial differential equations. In *International Conference on Learning Representations*, 2021.
- M. Louboutin, M. Lange, F. Luporini, N. Kukreja, P. A. Witte, F. J. Herrmann, P. Velesko, and G. J. Gorman. Devito (v3.1.0): an embedded domain-specific language for finite differences and geophysical exploration. *Geoscientific Model Development*, 12(3):1165–1187, 2019.

- Mathias Louboutin, Ziyi Yin, Rafael Orozco, Thomas J. Grady II, Ali Siahkoohi, Gabrio Rizzuti, Philipp A. Witte, Olav Møyner, Gerard J. Gorman, and Felix J. Herrmann. Learned multiphysics inversion with differentiable programming and machine learning. *The Leading Edge*, 42(7):474–486, 2023.
- Fabio Luporini, Mathias Louboutin, Michael Lange, Navjot Kukreja, Philipp Witte, Jan Hückelheim, Charles Yount, Paul H. J. Kelly, Felix J. Herrmann, and Gerard J. Gorman. Architecture and performance of Devito, a system for automated stencil computation. *ACM Transactions on Mathematical Software*, 46(1):6:1–6:28, 2020.
- Antonietta Mira, Reza Solgi, and Daniele Imparato. Zero variance Markov chain Monte Carlo for Bayesian estimators. *Statistics and Computing*, 23(5):653–662, 2013.
- Thomas Müller, Fabrice Rousselle, Alexander Keller, and Jan Novák. Neural control variates. *ACM Transactions on Graphics*, 39(6):243:1–243:19, 2020.
- Radford M. Neal. MCMC using Hamiltonian dynamics. In *Handbook of Markov Chain Monte Carlo*. Chapman and Hall/CRC, 2011.
- Chris J. Oates, Mark Girolami, and Nicolas Chopin. Control functionals for Monte Carlo integration. *Journal of the Royal Statistical Society: Series B*, 79(3):695–718, 2017.
- Chris J. Oates, Jon Cockayne, François-Xavier Briol, and Mark Girolami. Convergence rates for a class of estimators based on Stein’s method. *Bernoulli*, 25(2):1141–1159, 2019.
- Hyunwoo Oh. Training neural control variates using correlated configurations. *Physical Review D*, 112(7):074501, 2025.
- Rafael Orozco, Ali Siahkoohi, Mathias Louboutin, and Felix J. Herrmann. ASPIRE: iterative amortized posterior inference for Bayesian inverse problems. *Inverse Problems*, 41(4):045001, 2025.
- George Papamakarios, Eric Nalisnick, Danilo Jimenez Rezende, Shakir Mohamed, and Balaji Lakshminarayanan. Normalizing flows for probabilistic modeling and inference. *Journal of Machine Learning Research*, 22(57):1–64, 2021.
- Stefan T. Radev, Ulf K. Mertens, Andreas Voss, Lynton Ardizzone, and Ullrich Köthe. BayesFlow: Learning complex stochastic models with invertible neural networks. *IEEE Transactions on Neural Networks and Learning Systems*, 33(4):1452–1466, 2020.
- Danilo Jimenez Rezende and Shakir Mohamed. Variational inference with normalizing flows. In *International Conference on Machine Learning*, 2015.
- Christian P. Robert and George Casella. *Monte Carlo Statistical Methods*. Springer, 2nd edition, 2004.
- Gareth O. Roberts and Jeffrey S. Rosenthal. Optimal scaling of discrete approximations to Langevin diffusions. *Journal of the Royal Statistical Society: Series B*, 60(1):255–268, 1998.
- Shijing Si, Chris J. Oates, Andrew B. Duncan, Lawrence Carin, and François-Xavier Briol. Scalable control variates for Monte Carlo methods via stochastic optimization. In *Monte Carlo and Quasi-Monte Carlo Methods*, pages 205–221, 2022.
- Ali Siahkoohi, Gabrio Rizzuti, and Felix J. Herrmann. Deep Bayesian inference for seismic imaging with tasks. *Geophysics*, 87(5):S281–S302, 2022.
- Ali Siahkoohi, Gabrio Rizzuti, Rafael Orozco, and Felix J. Herrmann. Reliable amortized variational inference with physics-based latent distribution correction. *Geophysics*, 88(3):R297–R322, 2023.
- Yang Song and Stefano Ermon. Generative modeling by estimating gradients of the data distribution. In *Advances in Neural Information Processing Systems*, 2019.
- Leah F. South, Toni Karvonen, Christopher Nemeth, Mark Girolami, and Chris J. Oates. Semi-exact control functionals from Sard’s method. *Biometrika*, 109(2):351–367, 2022.
- Leah F. South, Chris J. Oates, Antonietta Mira, and Christopher Drovandi. Regularized zero-variance control variates. *Bayesian Analysis*, 18(3):865–888, 2023.
- Charles Stein. A bound for the error in the normal approximation to the distribution of a sum of dependent random variables. In *Proceedings of the Sixth Berkeley Symposium on Mathematical Statistics and Probability*, volume 2, pages 583–602, 1972.
- Andrew M. Stuart. Inverse problems: a Bayesian perspective. *Acta Numerica*, 19:451–559, 2010.
- Zhuo Sun, Alessandro Barp, and François-Xavier Briol. Vector-valued control variates. In *International Conference on Machine Learning*, 2023a.
- Zhuo Sun, Chris J. Oates, and François-Xavier Briol. Meta-learning control variates: variance reduction with limited data. In *Conference on Uncertainty in Artificial Intelligence*, 2023b.
- Albert Tarantola. *Inverse Problem Theory and Methods for Model Parameter Estimation*. SIAM, 2005.
- Ruosi Wan, Mingjun Zhong, Haoyi Xiong, and Zhanxing Zhu. Neural control variates for Monte Carlo variance reduction. In *European Conference on Machine Learning and Principles and Practice of Knowledge Discovery in Databases*, 2020.

A DERIVATION OF STEIN’S IDENTITY FOR POSTERIOR DISTRIBUTIONS

We provide a self-contained derivation of Stein’s identity (equation (4)) in the context of posterior distributions arising from Bayesian inverse problems. The derivation relies on the divergence theorem in \mathbb{R}^d and the product rule for divergences.

A.1 SETUP AND REGULARITY CONDITIONS

Let $p(\mathbf{x}|\mathbf{y})$ denote the posterior density over $\mathbf{x} \in \mathbb{R}^d$ for a fixed observation $\mathbf{y} \in \mathbb{R}^m$, and let $\phi(\mathbf{x}, \mathbf{y}): \mathbb{R}^d \times \mathbb{R}^m \rightarrow \mathbb{R}^d$ be a smooth vector-valued function. We require:

1. $p(\mathbf{x}|\mathbf{y})$ is continuously differentiable and strictly positive on \mathbb{R}^d ;
2. $\phi(\cdot, \mathbf{y})$ is continuously differentiable for each \mathbf{y} ;
3. The boundary condition $\lim_{\|\mathbf{x}\| \rightarrow \infty} \phi(\mathbf{x}, \mathbf{y}) p(\mathbf{x}|\mathbf{y}) = \mathbf{0}$ holds, ensuring that the surface integral at infinity vanishes.

The boundary condition is satisfied whenever $p(\mathbf{x}|\mathbf{y})$ decays sufficiently fast—e.g., when the prior is Gaussian or has sub-Gaussian tails—and ϕ grows at most polynomially.

A.2 DERIVATION VIA INTEGRATION BY PARTS

Consider the integral

$$I = \int_{\mathbb{R}^d} \nabla_{\mathbf{x}} \cdot [\phi(\mathbf{x}, \mathbf{y}) p(\mathbf{x}|\mathbf{y})] d\mathbf{x}, \quad (13)$$

where $\nabla_{\mathbf{x}} \cdot \mathbf{v} = \sum_{i=1}^d \partial v_i / \partial x_i$ denotes the divergence. By the divergence theorem applied to the ball $B_R = \{\mathbf{x} : \|\mathbf{x}\| \leq R\}$,

$$\int_{B_R} \nabla_{\mathbf{x}} \cdot [\phi p] d\mathbf{x} = \oint_{\partial B_R} [\phi p] \cdot \hat{\mathbf{n}} dS,$$

where $\hat{\mathbf{n}}$ is the outward normal to the sphere ∂B_R . By the boundary condition (3), the surface integral vanishes as $R \rightarrow \infty$, giving

$$I = \int_{\mathbb{R}^d} \nabla_{\mathbf{x}} \cdot [\phi(\mathbf{x}, \mathbf{y}) p(\mathbf{x}|\mathbf{y})] d\mathbf{x} = 0. \quad (14)$$

A.3 EXPANDING VIA THE PRODUCT RULE

We now expand the divergence in the above expression using the product rule. For each component i :

$$\frac{\partial}{\partial x_i} [\phi_i(\mathbf{x}, \mathbf{y}) p(\mathbf{x}|\mathbf{y})] = \frac{\partial \phi_i}{\partial x_i} p(\mathbf{x}|\mathbf{y}) + \phi_i(\mathbf{x}, \mathbf{y}) \frac{\partial p(\mathbf{x}|\mathbf{y})}{\partial x_i}.$$

Summing over $i = 1, \dots, d$ and using the identity $\nabla p/p = \nabla \log p$:

$$\begin{aligned} \nabla_{\mathbf{x}} \cdot [\phi p] &= \left(\sum_{i=1}^d \frac{\partial \phi_i}{\partial x_i} \right) p + \left(\sum_{i=1}^d \phi_i \frac{\partial p}{\partial x_i} \right) \\ &= (\nabla_{\mathbf{x}} \cdot \phi) p + (\phi \cdot \nabla_{\mathbf{x}} \log p) p. \end{aligned}$$

Substituting into equation (14) and dividing by p inside the expectation:

$$\mathbb{E}_{p(\mathbf{x}|\mathbf{y})} [\nabla_{\mathbf{x}} \cdot \phi(\mathbf{x}, \mathbf{y}) + \phi(\mathbf{x}, \mathbf{y}) \cdot \nabla_{\mathbf{x}} \log p(\mathbf{x}|\mathbf{y})] = 0, \quad (15)$$

which is exactly equation (4). This establishes that $g(\mathbf{x}, \mathbf{y}) = \nabla_{\mathbf{x}} \cdot \phi + \phi \cdot \nabla_{\mathbf{x}} \log p(\mathbf{x}|\mathbf{y})$ has zero expectation under the posterior for *any* ϕ satisfying the regularity conditions.

Component-wise identity. Since the divergence theorem applies to each component of ϕp independently, the identity also holds *per component* before summing:

$$\mathbb{E}_{p(\mathbf{x}|\mathbf{y})} \left[\frac{\partial \phi_j}{\partial x_j} + \phi_j \frac{\partial \log p(\mathbf{x}|\mathbf{y})}{\partial x_j} \right] = 0, \quad j = 1, \dots, d.$$

This justifies the vector-valued control variate in equation (8): each component $g_{\theta, j}$ independently has zero expectation, so $\mathbb{E}[g_{\theta}] = \mathbf{0}$ without requiring the components to sum.

A.4 APPLICATION TO COUPLING LAYER ARCHITECTURES

For our coupling layer parameterization (equation (6)), the divergence takes the explicit form (7). The triangular structure means $\nabla_{\mathbf{x}} \cdot \phi_{\theta}$ involves only the diagonal of the Jacobian, which equals 1 for untransformed components and $s_{\theta, i}(\mathbf{x}_1, \mathbf{y})$ for transformed components. The resulting control variate

$$g_{\theta}(\mathbf{x}, \mathbf{y}) = \underbrace{\sum_{i \in \mathbf{x}_2} s_{\theta, i}(\mathbf{x}_1, \mathbf{y})}_{\text{divergence (exact)}} + \underbrace{d_1 + \phi_{\theta}(\mathbf{x}, \mathbf{y}) \cdot \nabla_{\mathbf{x}} \log p(\mathbf{x}|\mathbf{y})}_{\text{score term}}$$

In the above expression, $d_1 = \dim(\mathbf{x}_1)$. This control variate satisfies $\mathbb{E}_{p(\mathbf{x}|\mathbf{y})} [g_{\theta}(\mathbf{x}, \mathbf{y})] = 0$ exactly, with no approximation in the divergence computation. This unbiasedness guarantee holds regardless of the neural network parameters θ (provided the boundary conditions are met), and is preserved under ensemble averaging (equation (9)).

For the hierarchical coupling layer, the recursive binary tree structure computes the Jacobian diagonal as $\text{diag}(\nabla_{\mathbf{x}} \phi) = [\mathbf{d}_{\text{upper}}; \mathbf{s} \odot \mathbf{d}_{\text{lower}}]$, where $\mathbf{d}_{\text{upper}}$ and $\mathbf{d}_{\text{lower}}$ are the diagonals from the upper and lower subtrees, and \mathbf{s} is the scale vector from the coupling at the current node. At leaf nodes, $\mathbf{d} = \mathbf{1}$. The divergence is then $\text{tr}(\nabla_{\mathbf{x}} \phi) = \mathbf{1}^{\top} \mathbf{d}$, which remains analytically computable and exact.

A.5 BOUNDARY CONDITIONS FOR POSTERIOR DISTRIBUTIONS IN INVERSE PROBLEMS

We verify that condition (3) holds in typical inverse problem settings. For a Gaussian prior $p_{\text{prior}}(\mathbf{x}) = \mathcal{N}(\boldsymbol{\mu}_0, \boldsymbol{\Sigma}_0)$ and Gaussian likelihood $p(\mathbf{y}|\mathbf{x}) = \mathcal{N}(\mathbf{x}, \sigma^2\mathbf{I})$, the posterior satisfies $p(\mathbf{x}|\mathbf{y}) \leq C \exp(-\frac{1}{2}(\mathbf{x} - \boldsymbol{\mu}_0)^\top \boldsymbol{\Sigma}_0^{-1}(\mathbf{x} - \boldsymbol{\mu}_0))$ for some $C > 0$, since the likelihood is bounded above by 1. This Gaussian tail decay ensures $\phi(\mathbf{x}, \mathbf{y}) p(\mathbf{x}|\mathbf{y}) \rightarrow \mathbf{0}$ as $\|\mathbf{x}\| \rightarrow \infty$ whenever ϕ grows at most polynomially—which holds for neural networks with bounded (tanh, sigmoid) or polynomially growing (ReLU) activations. For non-Gaussian priors such as the Rosenbrock density $\exp(-a(x_1 - \mu)^2 - b(x_2 - x_1^2)^2)$, the super-exponential decay in all directions similarly ensures the boundary conditions hold.

A.6 EMPIRICAL VERIFICATION

Figure 12 provides an empirical check of Stein’s identity. For each of 250 test observations \mathbf{y} , we draw $N = 5,000$ posterior samples and compute the dimension-averaged sample mean of the control variate, $\frac{1}{Nd} \sum_{i,j} g_j(\mathbf{x}_i, \mathbf{y})$, which should be zero by construction. Across all four experiments—Gaussian ($d = 4$, analytical score), Rosenbrock ($d = 2$), nonlinear ($d = 4$), and Darcy ($d = 100$, all three with learned scores)—this quantity is tightly concentrated around zero (mean ≈ 0 , std $\approx 10^{-3}$), confirming that the zero-mean guarantee holds in practice.

B PER-COMPONENT VARIANCE REDUCTION ON DARCY FLOW

Figure 13 shows the per-component VRF for each of the 100 KL coefficients, sorted by decreasing prior eigenvalue. Two regimes are visible:

Low-frequency modes (components 1–30). These modes correspond to large prior eigenvalues λ_j and carry most of the prior variance. Because the data strongly constrains these components, the posterior variance $\text{Var}(z_j|\mathbf{y})$ is already much smaller than the prior variance λ_j^2 . The control variate must match the posterior mean function $\mathbb{E}[z_j|\mathbf{y}]$ —a nonlinear function of the observation—which is harder for the leading modes where the data is most informative. This yields VRF close to 1.

High-frequency modes (components 60–100). These modes have small prior eigenvalues and are barely constrained by the data: $p(z_j|\mathbf{y}) \approx p(z_j) = \mathcal{N}(0, 1)$. Here the posterior score is dominated by the prior score $\nabla_{z_j} \log p(z_j) = -z_j$, which the coupling layers can approximate easily, yielding VRF as low as 0.04.

The component-averaged VRF is approximately 0.16, while

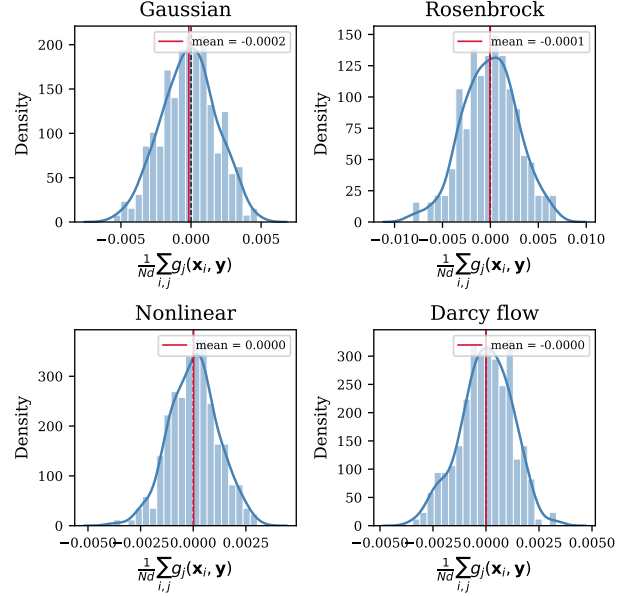


Figure 12: Empirical verification of Stein’s identity. Each panel shows the distribution of $\frac{1}{Nd} \sum_{i,j} g_j(\mathbf{x}_i, \mathbf{y})$ across 250 test observations ($N = 5,000$ samples each). All four distributions are centered at zero, confirming the zero-mean guarantee.

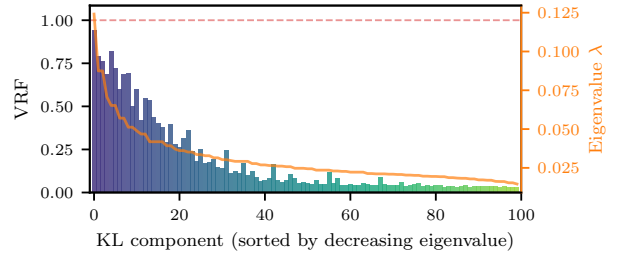


Figure 13: Per-KL-component VRF on the Darcy flow problem ($d = 100$), sorted by decreasing prior eigenvalue λ_j (orange curve, right axis). High-frequency modes (small λ_j , right side) achieve VRF as low as 0.04; low-frequency modes (large λ_j , left side) have VRF ≈ 1 . The dashed line marks VRF = 1 (no improvement).

the per-observation VRF reported in Section 4.2 (~ 0.18) aggregates differently across samples. In both cases, the overall reduction is substantial because the majority of components (those with smaller eigenvalues) achieve very low VRF.

C CNF QUALITY DIAGNOSTICS FOR DARCY FLOW

Since the Darcy flow experiment relies entirely on a learned CNF for both posterior sampling and score computation, we

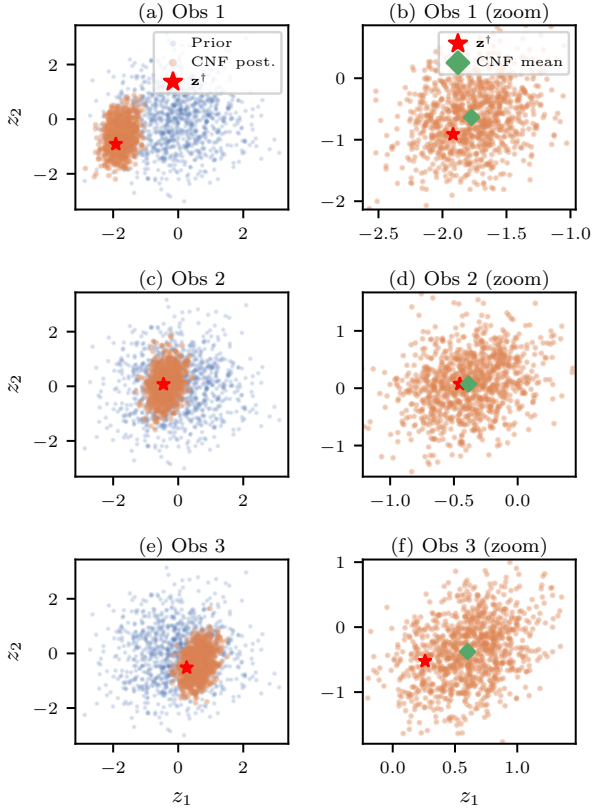


Figure 14: First two KL components of the CNF posterior for three held-out observations. Left column: prior samples (blue) and CNF posterior samples (orange) with the true parameter (red star); the CNF correctly concentrates around the truth. Right column: zoomed view showing the CNF posterior mean (green diamond) near the truth.

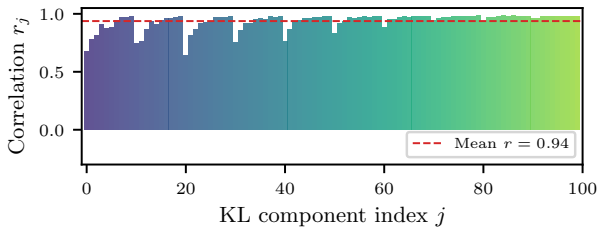


Figure 15: Per-component Pearson correlation between the CNF score $\hat{s}_j = \partial_{z_j} \log p_\varphi(\mathbf{z}|\mathbf{y})$ and the physics-based posterior score s_j (adjoint PDE + prior), evaluated at 100 held-out test observations. Mean $\bar{r} = 0.94$, median 0.97.

provide diagnostics verifying the quality of the trained CNF (Section 4.2).

Figure 14 projects the 100-dimensional posterior onto the first two KL components—i.e., those with the largest prior eigenvalues—for three held-out observations. In each case, the CNF posterior (orange) is correctly concentrated around

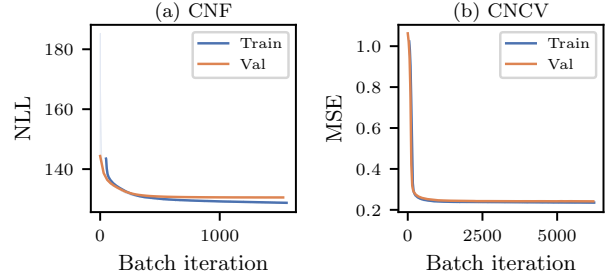


Figure 16: Training and validation loss curves. (a) CNF negative log-likelihood: raw per-batch training loss (light), smoothed training loss (dark), and validation NLL per epoch. (b) CNCV mean-squared error: same layout. Both models converge without overfitting.

the true parameter (red star), with the CNF posterior mean (green diamond) close to the truth. As expected, the prior samples (blue) are substantially more dispersed, confirming that the CNF has learned meaningful posterior concentration.

Figure 15 compares the CNF score $\nabla_{\mathbf{z}} \log p_\varphi(\mathbf{z}|\mathbf{y})$ against the physics-based posterior score computed via adjoint PDE solves and the GRF prior (Section 4.2), for each of the 100 KL components across 100 held-out observations. We observe that the per-component Pearson correlation is high (mean $\bar{r} = 0.94$, median 0.97), confirming that the CNF learns an accurate score across nearly all KL modes. We note that CNFs trained without weight decay ($\lambda = 0$) produced inaccurate scores due to coupling-scale explosion; weight decay of 10^{-4} on the AdamW optimizer was essential for stable training.

Figure 16 shows the training dynamics for both the CNF and the CNCV ensemble. Both models converge smoothly, with validation losses tracking the training losses closely, indicating no significant overfitting.

D ADDITIONAL DARCY POSTERIOR VISUALIZATIONS

Figure 17 shows posterior summaries for three additional held-out observations, demonstrating that CNCV generalizes beyond the single observation shown in Figure 10. Each row follows the same format: pressure field p^\dagger with sensor locations, true log-permeability u^\dagger , CNCV posterior mean, and posterior standard deviation. Across all observations, the CNCV posterior mean recovers the large-scale structure of the truth, with posterior uncertainty concentrated in the domain interior, away from sensors and Dirichlet boundaries.

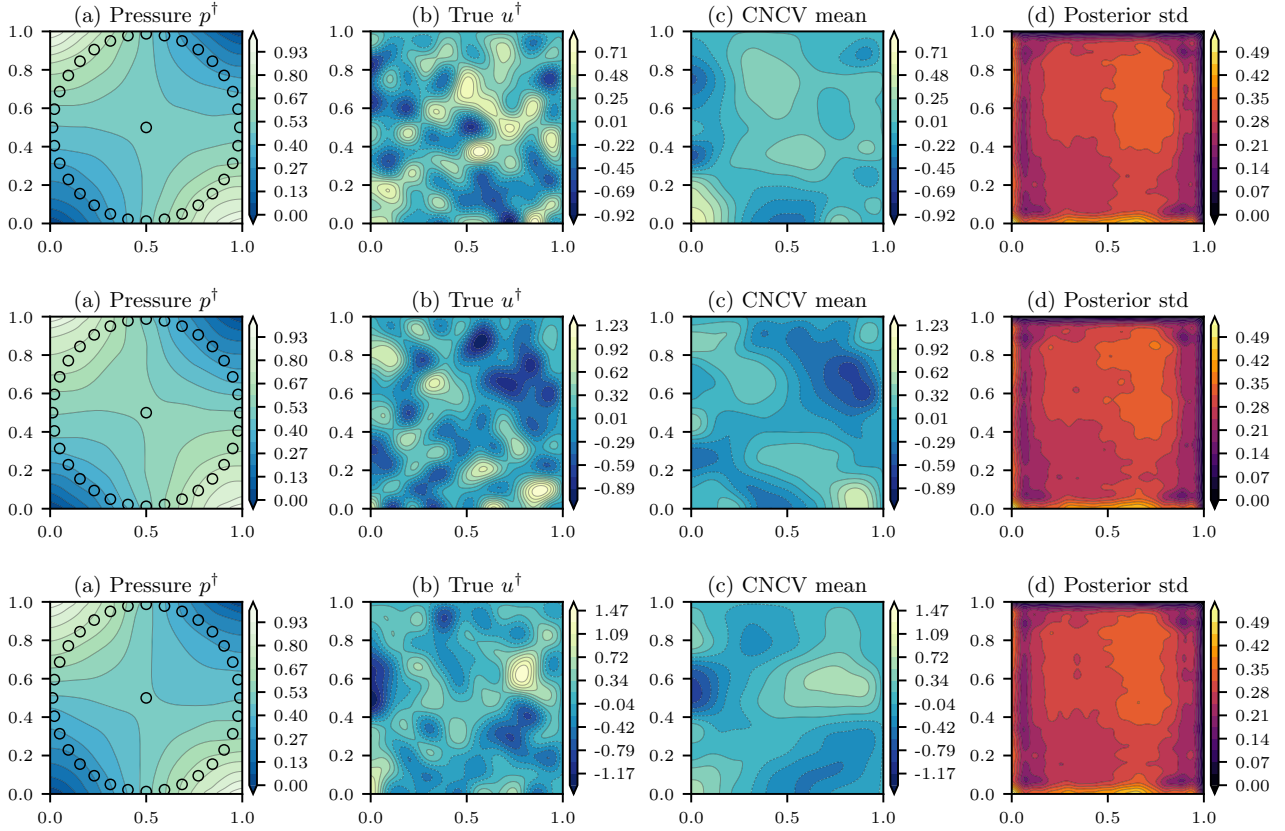


Figure 17: Darcy posterior summaries for three additional held-out test observations. Each row shows a different observation. Columns: (a) pressure p^\dagger with sensors, (b) true u^\dagger , (c) CNCV posterior mean, (d) posterior std.

E EXPERIMENTAL DETAILS AND HYPERPARAMETERS

We provide complete hyperparameter specifications for all experiments. All models are trained with the Adam optimizer [Kingma and Ba, 2015] unless otherwise noted (AdamW for the Darcy CNF). Learning rates follow a cosine schedule from lr_{init} to lr_{final} .

E.1 CNCV ENSEMBLE (SECTIONS 4.1 AND 4.2)

Table 3 summarizes the CNCV hyperparameters. The same architecture ($L = 16$, depth 2, 64 hidden, 3-layer MLP) is used across all stylized experiments; only the Darcy problem requires a deeper MLP (5 layers) and lower learning rate due to the higher dimensionality ($d = 100$).

E.2 CONDITIONAL NORMALIZING FLOWS (SECTIONS 4.1 AND 4.2)

Table 4 shows the CNF hyperparameters. The Gaussian and Rosenbrock CNFs use 12 flow layers with 128 hidden units, while the nonlinear CNF uses 8 flow layers with 64 hidden

Table 3: CNCV ensemble hyperparameters.

	Gauss.	Rosenb.	Nonlin.	Darcy
d	2–16	2	4	100
L (ensemble)	16	16	16	16
Tree depth	2	2	2	3
MLP layers	3	3	3	5
Hidden units	64	64	64	128
Batch size	2048	2048	2048	4096
Train samples	65,536	65,536	65,536	120,000
Epochs	50	50	100	400
lr_{init}	10^{-3}	10^{-3}	10^{-3}	10^{-4}
lr_{final}	10^{-4}	10^{-4}	10^{-4}	10^{-5}
Seed	12	1	12	12

units; all are trained on 262k joint samples. The Darcy CNF is substantially larger (12 flow layers, 128 hidden, 17.2M parameters) to handle the 100-dimensional KL space with 33-dimensional observations. Weight decay of 10^{-4} is applied only for the Darcy CNF, where it prevents coupling scale explosion (Appendix C).

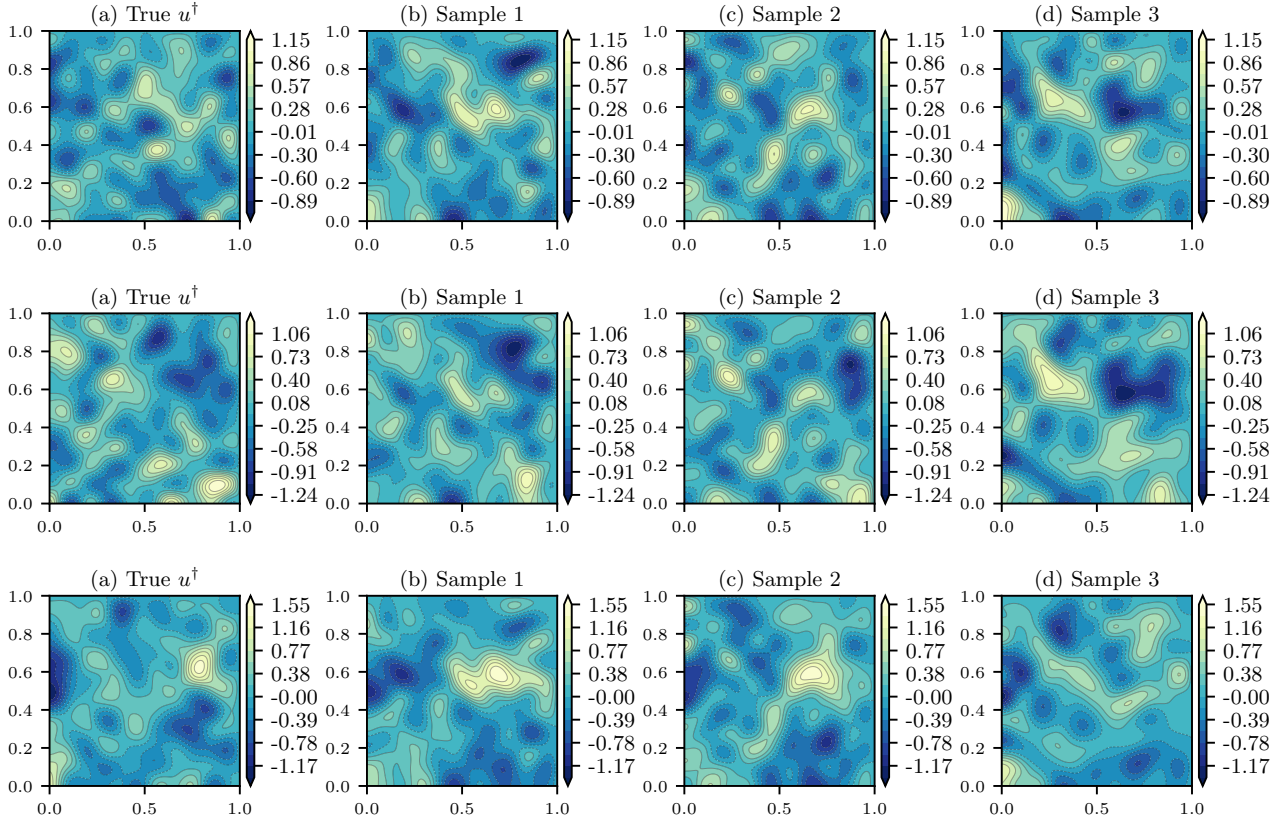


Figure 18: Individual posterior samples for the same three observations as Figure 17. Each row shows the true field (a) and three independent draws from the CNF approximate posterior (b–d). Samples preserve the frequency content of the truth; the smoothness of the posterior mean in Figure 17(c) arises from averaging over uncertain high-frequency modes.

Table 4: Conditional normalizing flow hyperparameters.

	Gauss.	Rosenb.	Nonlin.	Darcy
Flow layers	12	12	8	12
Tree depth	2	2	2	6
MLP layers	3	3	3	3
Hidden units	128	128	64	128
Batch size	8192	4096	8192	4096
Train samples	262,144	262,144	262,144	120,000
Epochs	1000	1000	1000	200
lr_{init}	10^{-3}	10^{-3}	10^{-3}	10^{-3}
lr_{final}	10^{-5}	10^{-5}	10^{-5}	10^{-5}
Weight decay	0	0	0	10^{-4}
Parameters	0.6M	0.2M	0.1M	17.2M

E.3 DIFFUSION MODEL FOR THE NONLINEAR EXPERIMENT

The denoising diffusion probabilistic model used for posterior sampling in the nonlinear experiment (Section 4.1) uses 1000 diffusion timesteps with a linear noise schedule $\beta_t \in [10^{-4}, 0.02]$. The denoising network is a 5-layer MLP with 512 hidden units, conditioned on the observation y via

concatenation and on the timestep via sinusoidal position embeddings. Training uses 65,536 joint samples, batch size 4096, and a cosine learning rate schedule from 10^{-3} to 10^{-4} over 1000 epochs.

E.4 COMPUTATIONAL COST

Training the CNCV ensemble takes approximately 5 minutes for the stylized experiments ($d \leq 16$) and 50 minutes for the Darcy problem ($d = 100$) on a single NVIDIA RTX 2000 Ada Generation GPU (16 GB). The Darcy CNF requires approximately 2 hours of training. At inference time, evaluating \mathbf{g}_{ens} for a batch of M samples requires $L = 16$ forward passes through the coupling layer networks plus M score evaluations. For the Darcy problem with $M = 200$ samples, inference takes ~ 0.5 s, compared to ~ 100 s for 200 PDE solves.